On the Role of the Plaque Porous Structure in Mussel Adhesion: Implications for Adhesion Control Using Bulk Patterning

Ahmed Ghareeb
Civil and Environmental Engineering,
University of Illinois at Urbana-Champaign,
2119 Newmark Civil Engineering Lab,
205 N. Mathews Ave,
Urbana, IL 61801
e-mail: ghareeb2@illinois.edu

Ahmed Elbanna[1]
Civil and Environmental Engineering,
University of Illinois at Urbana-Champaign,
2219 Newmark Civil Engineering Lab,
205 N. Mathews Ave,
Urbana, IL 61801
e-mail: elbanna2@illinois.edu

Mussel adhesion is a problem of great interest to scientists and engineers. Recent microscopic imaging suggests that the mussel material is porous with patterned void distributions. In this paper, we study the effect of the pore distribution on the interfacial-to-the overall response of an elastic porous plate, inspired from mussel plaque, glued to a rigid substrate by a cohesive interface. We show using a semi-analytical approach that the existence of pores in the vicinity of the crack reduces the driving force for crack growth and increases the effective ductility and fracture toughness of the system. We also demonstrate how the failure mode may switch between edge crack propagation and inner crack nucleation depending on the geometric characteristics of the bulk in the vicinity of the interface. Numerically, we investigate using the finite element method two different void patterns; uniform and graded. Each case is analyzed under displacement-controlled loading. We show that by changing the void size, gradation, or volume fraction, we may control the peak pulling force, maximum elongation at failure, as well as the total energy dissipated at complete separation. We discuss the implications of our results on design of bulk heterogeneities for enhanced interfacial behavior. [DOI: 10.1115/1.4041223]

1 Introduction

Mussel adhesion has been a problem of great interest to scientists and engineers over the past two decades [1,2]. Mussels achieve strong attachment, with high ductility, to organic and inorganic surfaces in harsh under-water environments. The byssus attachments enable the mussel to adapt to the lift and the drag of ocean waves [3]. Mussel adhesion has provided a unique model system to understand wet adhesion for biomimetic applications.

The Mussel adhesion problem has been extensively studied within the scope of physical chemistry. The natural adhesive proteins produced by the mussels play a major role in the adhesion. Identifying the composition of the protein was the focus of many prior studies [4–6]. Previous research showed that these proteins can bond to different materials including glass, wood, and concrete. Further studies have been conducted to identify the genes responsible for producing these adhesive proteins [7].

The role of mussel's material mechanical properties has also been partially investigated. Previous research suggests that the material properties vary for different mussels, and that the attachment strength may be enhanced by yield in plaque material before failure [8]. The details of the plaque shape, mechanics, and loading scheme were shown experimentally to be important in determining the adhesion strength and mode of failure [9]. Three modes of failure were reported experimentally: (i) Adhesive failure at the interface between the plaque and the substrate, (ii) interior cohesive failure of the plaque material within the center of the plaque under the thread–plaque junction, and (iii) exterior cohesive failure of the plaque material outside the center of the plaque where a tear propagates to the plaque–substrate interface. Cohesive failure within the plaque material occurs in cases of strong chemical bonding at the interface. This paper focuses primarily on investigating the first failure mode.

However, most studies focused on the biochemical properties of mussel plaque proteins and surface conditions, without considering the role of structural features of the byssus that may play a crucial role in enhancing the adhesion. Recent microscopy studies on the plaque collected from mussels living in different environments suggest that the plaque structure is porous, as shown in Fig. 1, and that the void pattern may vary from one environment to another in response to the severity of loading the mussel is subjected to [1]. Better understanding of the chemical, structural, and mechanical principles of mussel adhesion may lead to controlled synthetic systems with enhanced desirable proprieties, which may pave the way to the development of optimized materials with enhanced adhesion for technological and biological applications [10]. The focus of this paper is thus to understand the role of bulk porosity, a topic that has been largely overlooked in the literature, in controlling the strength, ductility, and toughness of adhesive interfaces in material systems inspired by mussel plaque.

2 Pulling of A Porous Plate: A Semi-Analytical Model

As a starting point for our analysis, we consider the problem of pulling a porous 2D plate with unit thickness attached to a rigid substrate. The plate material is assumed to be linear elastic, isotropic, and homogenous. The model does not allow damage in the plate material and failure occurs only due to detachment via adhesive failure at the interface [9]. Furthermore, the voids are assumed to have rectangular shape to simplify the analysis, but circular voids are considered later in the finite element analysis. The thickness of the strip adjacent to the interface is small compared to the void width. Cohesive zone model (CZM) is used to model the adhesion between the 2D plate and the substrate. The setup of the problem is shown in Fig. 2(a), and due to symmetry, we analyze only one half of the plate (Fig. 2(b)). An upward displacement is applied at the
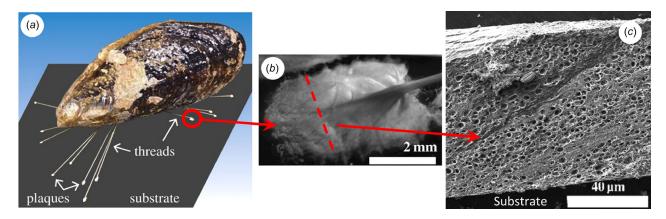
Fig. 1 The adhesive system in mussels: (*a*) a mussel attached to substrate by threads ending in plaques, (*b*) stereo micro-scope image of a M. californianus plaque under SEM, and (*c*) a cross section microscopic image of the plaque shows the porous structure of the bulk material and the variance of void sizes and distribution (Reproduced with permission from Fili-ppidi et al. [1], Copyright 2015 the Royal Society; permission conveyed through Copyright Clearance Center, Inc.).
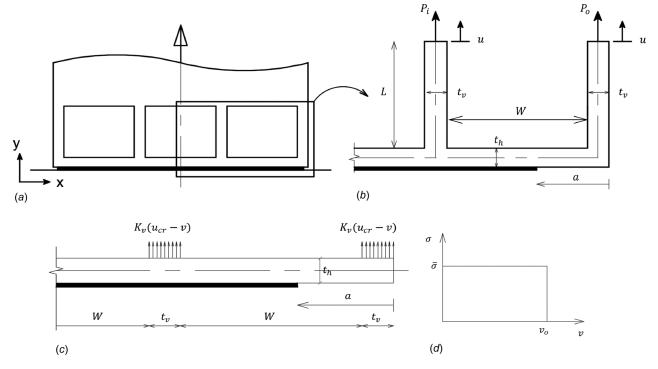

Fig. 2 Setup of the analytical model for the pulling a porous pillar attached to a rigid substrate: (*a*) The geometry of the 2D pil-lar with three near-interface rectangular voids, the pillar is subjected to an upward displacement, (*b*) the geometry and dimen-sions of the part of the pillar near the crack tip where the thickness of the horizontal strip is t_h, the thickness of the vertical strip is t_v, the void width is W, the void height is L, and the crack length a, (*c*) the simplified beam on elastic foundation model for the pillar with three rectangular voids, and (*d*) Dugdale's traction separation relation for the cohesive interface

upper edge of the plate. The displacements at the top of all vertical strips are assumed to be equal to u. The displacement in the x-direction is restrained on the right and left boundaries.

The plate is attached to the substrate through a Constant-strength (Dugdale) cohesive law as shown in Fig. 2(*d*). Due to the voids, the failure mechanism is changed from detachment of solid plate to peeling of the strip adjacent to the interface (the interfa-cial horizontal strip). Since this strip has a small height to length ratio, we idealize it as an Euler–Bernoulli beam on elastic founda-tion, whereas each vertical leg may be represented by a distributed stiffness $K_v = E/L$ representing the axial stiffness per unit area of the legs. The simplified model is shown in Fig. 2(*c*).

The differential equation governing the beam deformation is

$$\frac{d^4v}{dx^4} = \frac{w}{EI} \tag{1}$$

where v is the vertical deformation, E is Young's Modulus, I is the moment of inertia, and w is the distributed load per unit length. Referring to Fig. 3, the value of w applied upward is either $bK_v(u_{cr} - v)$ at the vertical webs locations or 0 under the void, and the value of w applied downward is either 0 at the debonded regions, or $b\bar{\sigma}$ at the damage zone. Since Dugdale's cohesive law is used, the bonded regions are assumed to be completely attached to the substrate ($v = 0$).

Equation (1) is solved at different values of crack length a to determine the process zone length l and the critical dis-placement u_{cr} required for unstable crack propagation at each value of that crack length. We investigate two scenarios for interfacial separation: (i) propagation of edge crack, and (ii) Initiation of local cracks under the vertical webs. The two cases are shown in Fig. 3. The solution details are shown in Appendix.
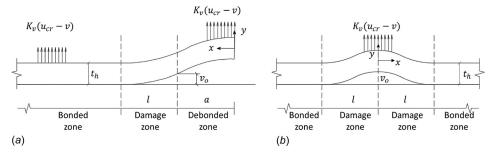
Fig. 3 Different cases of crack propagation under the elastic beam: (*a*) edge crack propagates under the void and (*b*) onset of local crack initiation under the inner leg

After calculating the values of u_{cr} and the constants for v, the total force in the outer and inner legs for the case of edge crack propagation is calculated by numerical integration as follows:

$$P_o = \int_0^{t_v} \frac{bK_v}{EI}(u_{cr} - v(x))dx \qquad (2)$$

$$P_i = \int_{W+t_v}^{W+2t_v} \frac{bK_v}{EI}(u_{cr} - v(x))dx \qquad (3)$$

And the total force is

$$P = P_i + P_o \qquad (4)$$

And for local crack initiation (Fig. 3(*b*)), we calculate the critical force value

$$P_i = \int_{-t_v/2}^{t_v/2} \frac{bK_v}{EI}(u_{cr} - v(x))dx \qquad (5)$$

Results of the Semi-Analytical Model. We solve the equations using the following set of parameters: For the porous plate, the Young's modulus $= 500$ MPa [8], and Poisson's ratio $= 0.45$. For the cohesive law, a constant stress (Dugdale) cohesive law is used with $\bar{\sigma} = 10$ MPa and $v_o = 0.075$ mm such that the cohesive fracture energy $= 750$ J/m^2 [11]. In addition, we consider a model setup as shown in Fig. 2(*a*) and numerically simulate its pulling response using finite element analysis with the same modeling parameters to test the predictions of the approximate analytical model. The displacements at the top of the plate and the top of the two vertical ribs were compared to check the validity of the assumption that they are equal. The difference in all modeled cases was less than 5%. Furthermore, the results were verified to be independent of mode mixity consistent with other studies for a similar geometry [11].

(i) Force-displacement

The relation between crack length and corresponding forces is plotted in Fig. 4(*a*). The semi-analytical results show that the total force decreases initially, then increases again till the crack propagates closer to the inner leg leading to a drop in the force. The increase in the force suggests that the system still loads while the crack propagates. Furthermore, a good agreement between the analytical and numerical solutions is observed. The two solutions perfectly match in the middle zone. There is an error of order of 10% in the force value when the crack tip is at the location of the vertical strip. This is due to approximating the vertical strips as axially loaded springs only and neglecting their rotational stiffness.

(ii) Effect of horizontal interfacial strip thickness and void width

To study the effect of the thickness (i.e., bending stiffness) of the interfacial horizontal strip, the total force versus crack length relation is plotted for various values of t_h/t_v as shown in Fig. 4(*b*). The plot shows that decreasing the thickness ratio results in higher drop in the force. However, in this limit, the force starts to increase at smaller values of a, and the slope of this loading part is higher. Also, the force required to propagate the crack under the inner leg increases with reducing the interfacial horizontal strip thickness.

Figure 4(*c*) shows the effect of increasing the void width, which leads to higher force in the inner leg and hence higher total force. This is true as long as local cracks have not initiated under the inner leg (Fig. 3(*b*)). These results suggest that reducing the thickness of the interfacial horizontal strip, or increasing the void width, amplifies the effect of the voids on crack propagation by redistributing the forces and channeling the strain energy away from the crack tip. For all the cases shown in Figs. 4(*b*) and 4(*c*), the increase in force is associated with an increase in the total displacement at failure and hence increase in total fracture toughness.

(iii) Different failure criteria

Figure 4(*d*) shows the relation between the maximum force in the inner leg and the interfacial horizontal strip thickness from analytical and numerical solutions for two values of void width W. The solid lines are from the analytical solution and the dashed lines are from the finite element solution. The figure illustrates the two different failure criteria: (i) the edge crack propagation and (ii) the initiation of local cracks under the inner vertical legs, discussed analytically in this section. For the failure mode where edge crack propagates, decreasing interfacial horizontal strip thickness delays the crack propagation leading to higher force in the inner legs. However, when the stresses under those legs exceed the cohesive strength, local separation initiates. The force required to initiate local separation increases with increasing the thickness of the interfacial horizontal strip. Increasing the void width increases the force and shifts the boundary between the two failure modes to the right as the void effect increases.

While the analytical solution presented in this section is approximate, it illustrates a central result of this paper: when a void is introduced close enough to the interface, and this notion of closeness will be made precise in Sec. 4, the force-crack length curve (*R*-curve) changes its qualitative trend as shown in Fig. 4(*a*). In particular, the macroscopic pulling force increases with crack length instead of decreasing as in the case of pulling a solid homogenous plate. In Secs. 3 and 4, we present detailed numerical simulations of this phenomenon and further analyze how patterning voids in the vicinity of an interface may lead to stress
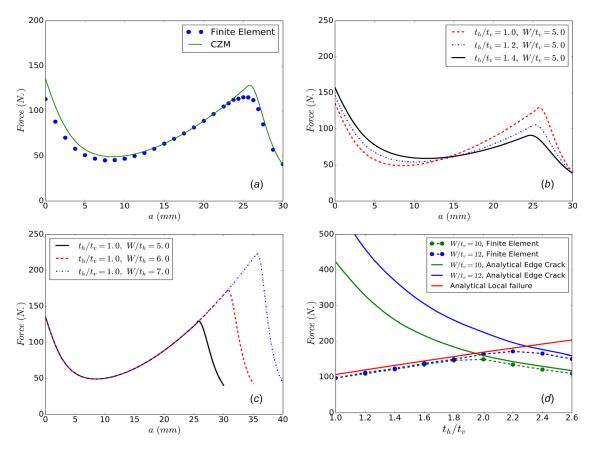
Fig. 4 Results from the approximate analytical model and finite element simulations: (a) force versus crack length from analytical and numerical solutions for $t_h = 5$ mm, $t_h/t_v = 1.0$, $W/t_h = 5.0$ showing that the total force may continue to increase even though the crack is expanding, (b) force versus crack length for the analytical model for various values of the interfacial horizontal strip to vertical web thickness ratio t_h/t_v and the same void width, (c) force versus crack length for the analytical model for the same interfacial horizontal to vertical strip thickness ratio t_h/t_v and various values of void width, and (d) maximum force in the inner leg versus interfacial horizontal strip to vertical strip thickness ratio for two different values of W/t_v from both the numerical and analytical solutions

inhomogeneity at the interface and slow down or trap the crack leading to more stretchability and increased apparent toughness of the system.

3 Plate With Circular Voids: Numerical Model Setup

Figure 5 shows the setup of our numerical model. It is composed of three parts: (i) a rigid base plate that represents the substrate, (ii) a porous plate that mimics the mussel's plaque
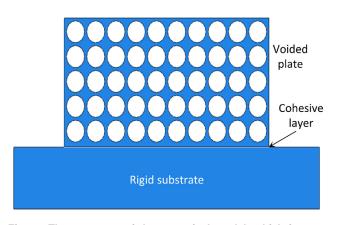

Fig. 5 The geometry of the numerical model, which is composed of a porous plate attached to a rigid substrate, throws a zero-thickness layer of cohesive material

material, and (iii) a zero-thickness cohesive layer joining the two components to represent the cohesion between the plate and the substrate. The dimensions of the base plate are chosen in a way that its boundaries have no effect on the results. The lower edge of the base plate is restrained from movement in both directions. A uniform upward displacement is applied at the top edge of the porous plate, to mimic the displacement applied on the mussel plaque through the thread.

To model the cohesive interface, we use a zero-thickness cohesive element. We adopt a simple intrinsic triangular cohesive law for mode I fracture composed of a linear elastic part up to the critical cohesive stress σ_{cr}, followed by linear degradation that evolves from crack initiation to complete failure. The analytical expression for the cohesive law is given by Furgiuele et al. [12]

$$\sigma(\Delta) = \begin{cases} K_o\Delta, & \Delta \leq \gamma\Delta_f \\ \sigma_{cr}(\Delta_f - \Delta)/(\Delta_f - \gamma\Delta_f), & \gamma\Delta_f \leq \Delta \leq \Delta_f \\ 0, & \Delta \geq \Delta_f \end{cases} \quad (6)$$

where K_o is penalty stiffness of the cohesive law, Δ_f is the failure (total separation) normal displacement, and γ is the ratio between the critical and the failure normal displacements. K_o value can be determined by selecting proper values of σ_{cr} and γ. The total area under the curve is the cohesive fracture energy G_c, and the length on which stress changes from σ_{cr} (initiation of degradation) to 0 (total separation) defines the process zone length l, which is related to the characteristic length L_{ch} of the cohesive zone law given by Ha et al. [13]:
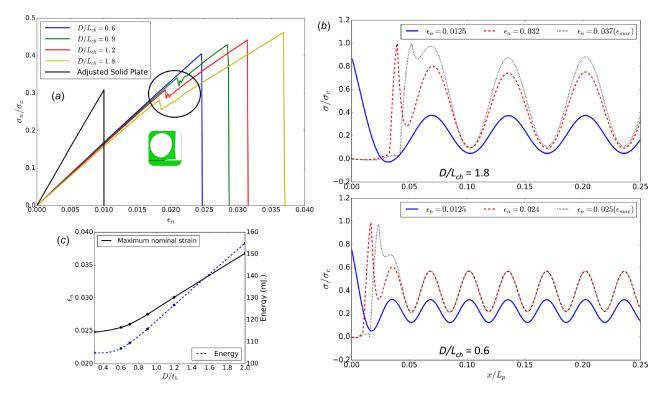
Fig. 6 Effect of void size: (*a*) normalized nominal stress versus nominal strain curves for the different plates with uniform voids. The void diameter to characteristic length ratios are listed in the legend. The result for a solid plate with the same material volume and in-plane dimension (but reduced thickness, i.e., reduced contact area) is also added for reference, (*b*) Normalized stress distribution along the interface at different nominal strain levels: (top) case of uniform voids with $D/L_{ch} = 1.8$, and (bottom) Case of uniform voids with $D/L_{ch} = 0.6$, and (*c*) maximum stretch and total energy versus relative void size.

$$L_{ch} = \frac{EG_c}{\sigma_{cr}^2} \qquad (7)$$

where E the is young's modulus of the bulk material, G_c is the cohesive model energy release rate, and σ_{cr} is the maximum allowed stress. This is a fundamental length scale in our problem that controls the solution dependence on the combination of material properties.

The width of the plate L_p is chosen to be at least 20 times the characteristic length of the cohesive zone. A notch of a length a_o is introduced at the edge of the interface to initiate the separation. Here, we have chosen a_o to be equal to 0.05 of the characteristic length. We use the finite element software package ABAQUS [14]. We conduct Implicit dynamic analysis with slow loading rate to represent a quasi-static pulling test under displacement-controlled boundary conditions. The porous plate is meshed using 2D plane strain quadrilateral elements, whereas the cohesive interface is meshed using zero thickness cohesive elements. The size of the cohesive elements is chosen to be $L_{ch}/50$ at most to ensure numerical stability and convergence [15]. We have conducted a mesh sensitivity analysis to insure adequate accuracy.

All simulations presented in this section, unless otherwise stated, have been run using the following set of parameters: For the porous plate the Young's modulus = 500 MPa [8], and Poisson's ratio = 0.45. For the cohesive law the critical cohesive stress = 10 MPa, cohesive fracture energy = 750 J/m2, and $\gamma = 0.5$. [11].

4 Numerical Model Results

Here, we consider the effects of void size, pattern, and volume fraction on the force displacement response, stress distribution on the interface, as well as the apparent fracture toughness for the setup shown in Fig. 5. In all cases considered here, the plates have the same material properties, and the same in-plane external

dimensions. The only controlled parameter is the void size and the material volume; all other geometric parameters are adjusted accordingly.

Effect of Void Size D. We normalize the void sizes by the characteristic length of the cohesive law. The nominal stress is calculated as the total plate force divided by the interfacial contact area, and the nominal strain is calculated as the top vertical displacement divided by the total plate height in the undeformed configuration. All length scales are normalized by the characteristic length of the cohesive law (L_{ch}), and all stress measures are normalized by the cohesive strength (σ_{cr}).

The nominal stress–strain curves for five models are compared to the adjusted results of a solid plate in Fig. 6(*a*). The solid plate has the same in-plane dimensions as the porous plates but different thickness so that the material volume is the same. It is observed that all tested porous plates give higher peak force and stretchability (maximum deformation) than the solid plate for the same solid material volume and in-plane dimensions. With increasing the void size relative to characteristic length, separation initiates at lower displacement values. This corresponds to the first stress drops in the stress strain curve. However, the crack slows down as it propagates beneath the first void allowing further increase in load. The overall stretchability for larger voids is higher. The crack slow-down effect is not noticed for the case of small void sizes, ($D/L_{ch} = 0.6$); the crack propagates continuously with no increase in force once the peak force is achieved. The effective elastic stiffness for all porous plates is nearly the same. The ultimate nominal stress increases slightly with increasing the void size.

To analyze these results, the stress distribution at the interface is plotted for two extreme cases: large void sizes ($D/L_{ch} = 1.8$) and small void sizes ($D/L_{ch} = 0.6$) at different nominal strain levels. Figure 6(*b*) (top) shows the evolution of stress distribution at the interface for the case of larger void sizes; the stresses under
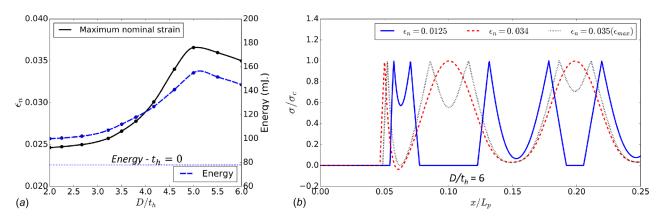
Fig. 7 Effect of void size to interfacial horizontal strip thickness ratio: (*a*) the maximum stretch and total energy versus void diameter to interfacial horizontal strip thickness ratio and (*b*) normalized stress distribution along the interface at different nominal strain levels for.$D/t_h = 6$

the vertical webs are high, whereas the values of stress under the voids are much smaller. At the beginning of loading, the stresses are high at the edges. This is where separation initiates. However, due to existence of low stress areas, the separation rate slows down allowing more compliant behavior. Thus, the strong stress inhomogeneity at the interface enables achieving higher stretch levels without significant reduction in maximum strength. The inhomogeneous propagation of interfacial separation also explains the small force drops observed in Fig. 6(*a*), where each drop corresponds to the progression of separation followed by a loading phase corresponding to a transient arrest (or to a slowing down phase).

For the case of small void sizes shown in Fig. 6(*b*) (bottom), the stress values are not varying significantly over the interface. The stress fluctuations about the mean value in this case are smaller than that observed for the large void case. As a result, after the separation initiates at the edge, it propagates faster than the previous case. This leads to complete separation at a lower stretch level.

Figure 6(*c*) shows that the maximum stretch scales nearly linear with the void size when the void diameter is larger than process zone length. Larger void sizes result in higher stretchability (for the same value of void volume fraction). Decreasing void size relative to the process zone length significantly reduces the void effects on stress distribution and stretchability. For voids with diameters much less than the process zone length, the void effect on the stress field is minor and the stress distribution at the interface is nearly constant (not shown here). Thus, as the void size decreases, the maximum nominal strain, at complete separation, approaches a constant value. The total energy, computed as the area under the stress strain curve, is also plotted in Fig. 6(*c*) and it shows similar trend as the maximum strain. As the void size increases, the total energy to failure also increases.

The numerical results suggest that increasing the void size compared to the interfacial horizontal strip thickness enhances the interfacial toughness by amplifying the void effect. However, reducing the adjacent strip thickness to zero will require, theoretically, infinite force for the edge crack propagation mode. Hence, the failure mode changes to the initiation of local cracks under the inner vertical webs and the overall strength and energy dissipation decreases. Figure 7(*a*) shows this nonmonotonic response. The maximum nominal strain and the total energy start decreasing when D/t_h exceeds 5, which mark the change in failure mode from edge crack propagation to initiation of local cracks under the webs for the specific material properties and geometric parameters used. The total energy value when $t_h = 0$ is shown on the same plot. For large D/t_h ratios, the local crack initiation under the vertical webs "fibrils" is shown in Fig. 7(*b*). The existence of the horizontal strip allows for stress redistribution and contributes to the

stress heterogeneity on the interface. Thus, the overall response may be optimized by tuning the thickness of the interfacial strip. These numerical results agree with the analytical model results shown in Fig. 4(*d*).

Effect of Void Pattern. Two different cases are modeled to study the effect of gradation of void sizes on the effective nominal stress–strain curve. In both cases, the plates have the same material volume as the plates with uniform voids studied before. The first plate has voids graded from $D/L_{ch} = 0.7$ at the interface to $D/L_{ch} = 1.2$ at the top. The second plate has voids graded from $D/L_{ch} = 1.2$ at the interface to $D/L_{ch} = 0.7$ at the top.

Figure 8(*a*) shows that when the gradation starts from larger voids near the interface to smaller voids further up, both maximum stretch and ultimate force increase. Furthermore, we compare each of the two graded models to the cases with uniform void sizes, where the constant void size is chosen equal to the void size in the row closest to the interface in the graded model. The results suggest that the stretchability has increased but the stiffness has decreased in both the graded cases compared to the corresponding uniform cases.

To further investigate the effect of void gradation, the stress distribution at the interface is plotted for the two graded designs as shown in Fig. 8(*b*). For the graded case where larger voids are placed closest to the interface, Fig. 8(*b*) (top) shows that the stress distribution is similar to the case of uniform large voids in the sense that there exist large stress fluctuations. This strong heterogeneity enables higher stretchability and increased resistance as the rupture may not propagate coherently but is forced to slow down or stop in regions with low stress. However, some differences between the graded and uniform cases exist. For example, the development of local depressions in the stress peaks, in the case of graded voids, suggests that multiple small cracks start to initiate locally under the webs, leaving intact zones in between the voids. This disintegration of the rupture process further toughens the interface and increases the deformation capacity.

The case of graded voids is similar to the case of functionally graded materials with graded elasticity modulus. Regions with larger pores represent more compliant regions, whereas regions with smaller pores represent stiffer regions. The observed results suggest that grading the pores from larger near the interface to smaller away from the interface, i.e., grading the elasticity modulus from smaller near the interface to larger away from it, enhances the behavior. This is similar in principal to Gibson-soil-like materials where graded elasticity was found to enhance flaw tolerance in the adhesive interfaces [16].

For the case of smaller voids near the interface shown in Fig. 8(*b*) (bottom), the behavior is similar to the case of uniform
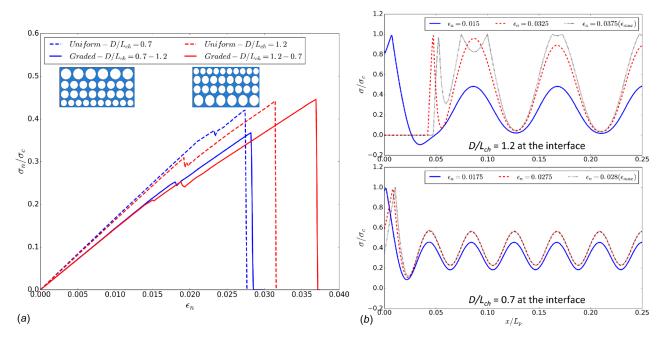
Fig. 8 Effect of void pattern: (a) normalized nominal stress versus nominal strain curves for the two plates with graded voids, the plates geometries are shown in the legend, also the normalized nominal stress versus nominal strain for two plates with equal void sizes $D/L_{ch} = 0.7$, and $D/L_{ch} = 1.2$ are added for comparison, and (b) normalized stress distribution along the interface at nominal strain levels: (top) case of graded voids with larger voids ($D/L_{ch} = 1.2$) at the interface, and (bottom) case of graded voids with smaller voids ($D/L_{ch} = 0.7$) at the interface

small voids in the sense that stress fluctuations are small. The lower part of the plate is stiffer and thus exhibits limited deformability compared to the case with larger voids near the interface.

The above results indicate that the maximum strength of the porous plate is primarily controlled by the stress distribution under the vertical webs, which is affected by the size of the voids closest to the interface. The maximum deformation, on the other hand, is more sensitive to the fluctuations in stress distribution on the interface as well as the bulk compliance, which depends on the void distribution throughout the whole plate.

Effect of Void Volume Fraction. To study the effect of voids volume fraction, the force displacement curves for three different volume fractions are plotted in Fig. 9, the plates have the same
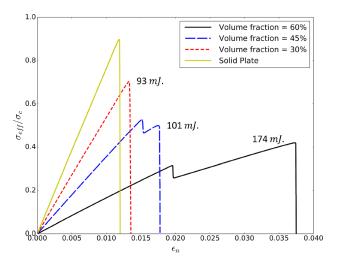

Fig. 9 Numerical results for plates with uniform voids for three different voids volume fraction 60, 45, and 30%. The numbers in the plot indicate the total area under the curve. The case of solid plate is added for reference.

number of voids, but the diameters are changed to change the volume fraction. The case of solid plate (0% volume fraction) is added for reference.

It is shown that with decreasing the volume fraction, the peak force increases but the peak displacement and the total area under the curve decrease. Increasing the void volume fraction corresponds to increasing the void size and reducing the spacing between the voids. Larger spacing corresponds to longer segments of the interface that are subjected to uniformly high stress, leading to lower ductility and brittle failure. On the other hand, increasing the void size increases the compliance of the plate and helps slowing down the crack propagation under the void leading to higher stretchability and thus higher energy dissipation until the limits discussed in Fig. 7(a) are probed.

Energy Budget. The results in this section show that patterning voids in the bulk affect the interfacial response. If compared with a solid plate with the same material volume and outer dimensions, a plate with voids gives higher peak force and stretchability in all studied cases. This suggests that the distribution of voids in the bulk, even in cases with the same effective bulk properties, may influence the energy release rate for the interfacial crack changing the effective toughness of the interface.

To demonstrate this, the strain energy of a plate with equal-sized voids (D/L_{ch} ranging between 0.6 and 1.8) is plotted against separation length as shown in Fig. 10(a). The nominal stress–strain curves for these cases are shown in Fig. 6(a).

Figure 10(a) shows that in the case of uniform small voids the strain energy reaches its peak (which corresponds to the peak force) at a small value of interfacial separation length and then monotonically decreases with increasing the separation length. However, the case of large voids is different. The strain energy decreases with the initiation of separation first. This continues until the crack reaches the low stress zones where it significantly slows down allowing the energy to increase again. This transient increase in the energy corresponds to a period of strain accumulation in the bulk while the interfacial separation continues propagating. This leads to higher stretchability before failure. After the
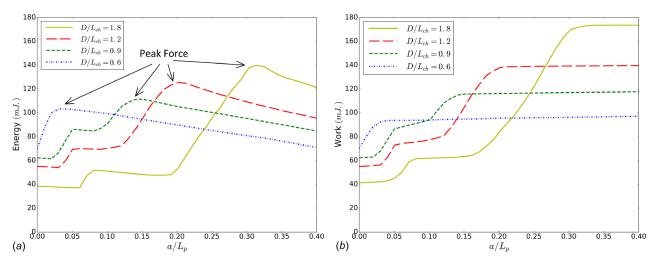
Fig. 10 Comparison of strain energy and external work versus separation length for plates with different void diameter to characteristic length ratios: (a) strain energy of the whole plate versus separation length along the interface, and (b) the total cumulative external work exerted on the plate versus separation length along the interface

strain energy reaches a peak value, it starts decreasing again as the separation dynamically propagates along the interface.

Figure 10(b) shows the cumulative external work exerted on the plates for different void sizes. The figure shows that with increasing the void size, the work keeps increasing for longer separation length allowing the plate to gain higher strain energy till it reaches the maximum value at the peak force. After this, the crack starts propagating dynamically. Since the CZM assumes the energy release rate in the cohesive layer is constant and equals to G_c, the high strain energy cannot be balanced only by the dissipated energy in the cohesive layer and kinetic energy starts to appear.

In Fig. 11, the components of the total energy are plotted for a plate with uniform voids of size $D/L_{ch} = 1.8$. The interfacial separation proceeds in two phases. The first phase is before reaching the peak force where the external work is partitioned between strain energy and energy dissipated by the cohesive interface during separation. This is a phase of quasi-static crack growth. The second phase is a phase of dynamic propagation after the peak force has been achieved. In this phase, the total strain energy of the plate decreases with crack propagation and a fraction of the strain energy is transformed into kinetic energy. The kinetic

energy magnitude increases with increasing the void size as the stored energy in the plate at the beginning of dynamic growth is higher.

This analysis of energy budget supports the earlier observations that the toughening effect of voids may be attributed to the resulting inhomogeneous crack growth. There are episodes of crack growth in which there is a net increase in the bulk strain energy and the external work rate is not constant. In these intervals, the energy is dissipated along the interface at a reduced rate. To see this, we recall that the rate of energy dissipation along the interface is given by

$$\frac{\partial E_f}{\partial a} = \frac{\partial E_f}{\partial t} \frac{\partial t}{\partial a} = \frac{1}{c} \frac{\partial E_f}{\partial t} \qquad (8)$$

where E_f is the dissipated energy by fracture, and c is the crack propagation speed.

From Fig. 11, $\partial E_f / \partial a =$ constant and from the prior discussion on the role of stress inhomogeneity in slowing down the rupture when propagating underneath the voids (i.e., c gets reduced) we may conclude that $\partial E_f / \partial t$ decreases in these regions enabling the plate to store more elastic energy and to stretch longer.

5 Discussion

The primary result of this paper is that bulk heterogeneities may change interfacial toughness. For the same intrinsic adhesive properties of the interface, we may get higher ductility and dissipated energy by changing the bulk structure. This may shed new lights in the mechanics of adhesion in mussel plaque beyond the role of interfacial physical chemistry. It is shown that a porous plate gives higher peak force and exhibits more stretchability than a solid plate with the same material volume and in-plane dimensions. The peak force depends primarily on the contact area, whereas the maximum elongation at failure depends mainly on the stress distribution at the interface and bulk stiffness; both are strongly dependent on the distribution of the voids in the bulk.

The effect of the stress distribution along the interface on the peak force and the maximum displacement at failure is evident from the cases investigated in the paper. Plates with larger voids have stronger stress heterogeneity than plates with smaller ones. The stronger the stress heterogeneity, the earlier the initiation of the separation at edges where the stress is more concentrated. This may cause a slight reduction, in general, in the peak elastic force compared to cases where the stress is less heterogeneous. However, regions of low stress may lead to slowing down of the separation, thus allowing higher stretchability.
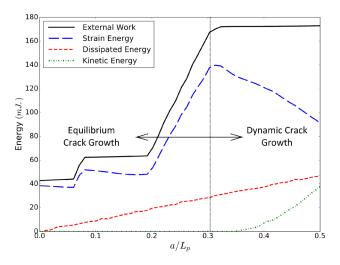

Fig. 11 Energy components of the plate during the growth of the interfacial separation versus separation length along the interface for a plate with uniform distribution of voids with $D/L_{ch} = 1.8$

Stress distribution at the interface is affected by the size and distribution of the voids, the continuity of the vertical webs, and the width of the horizontal strip near the interface. While the voids closest to the interface have a major effect on the peak force and maximum elongation, the gradation may further enhance the response. For the cases studied, we have found that having larger voids closer to the interface and smaller ones further away increases both the maximum force and elongation more than the other way around. Furthermore, the void effect is stronger if the void diameter is larger than the process zone size and if the thickness of interfacial horizontal strip is smaller than the process zone size.

The heterogeneities in the current study take the form of voids of different sizes. However, we hypothesize that similar conclusions may be drawn for solid inclusions instead and some recent work [17–19] has shown promising results in that direction. The mechanism enabling this effect is the influence of heterogeneity patterning on the strain energy distribution and consequently the energy release rate of the crack propagating along the interface. Furthermore, by investigating the energy partitioning during crack growth, we have shown that the rate of energy dissipation on the interface decreases during propagation underneath the voids enabling the plate to store higher levels of strain energy and to stretch longer. This opens new opportunities for altering interfacial response without changing the surface physical chemistry but through the introduction of near-interface voids.

Classically, enhancing interfacial toughness has been considered within the scope of problems in physical chemistry. By properly functionalizing the interface, properties like wetting, contact angle, and adhesion energy may be controlled [2,20]. Over the last two decades, it became clear that mechanics plays as much an important role in this problem as chemistry. In particular, there has been a surge of interest in patterning interfaces by introducing periodic [21–23] or functionally graded inclusions along the surfaces [24]. The nonuniformity of the fracture energy along the interface may be leveraged to enhance the interfacial resistance to separation and delamination by increasing the effective toughness [25].

Alternatively, some recent numerical studies suggest increasing interfacial adhesion by optimizing the distribution of interfacial stresses inspired by the biological example of fibrils with mushroom-shaped tips [26,27]. The simulations suggest that reducing the stress magnitude at the corner points, which initiates the crack propagation, significantly improves the interfacial adhesion [28,29]. This idea was demonstrated using a composite fibril composed of a stiff stalk and a soft tip rounded layer to decrease the corner stress [30]. That work suggested new opportunities for addressing the adhesion problem by manipulating bulk composition rather than changing interfacial properties. Here, we extend this idea to consider the case of porous materials glued to an interface since porous structures exist pervasively in engineering and natural materials.

There is extensive literature on void growth as a toughening mechanism in viscoplastic solids [31,32] and bonded elastic layers including for example the problem of peeling of duct tapes. Experimental studies show that one failure mode is associated with cavitation in the adhesive layer and formation of fibrils [33,34]. The cavitation/fibril formation processes help dissipate energy and thus increases toughness. However, the void formation and growth in these cases remain largely stochastic and susceptible to internal defect distributions. A systematic design for the voids from the beginning, as proposed here, may achieve better toughening results with a higher level of control. This may be particularly relevant for improving adhesion in soft polymeric materials including emerging ones such as hydrogels.

Future extension of this study may include studying the effect of void shape beyond the circular case investigated here as well as the effect of bulk material nonlinearity and the possible tradeoff between initiating failure in the bulk material versus separation at the interface. We also hope that this work may inspire new experimental work, which is needed to directly quantify the characteristic length of the plaque adhesion (Eq. (7)) and thus determine, for different types of mussels, what range of values of D/L_{ch} may be most relevant. This will further contribute to our understanding of failure mode selection mechanism in these complex systems.

6 Conclusions

In this paper, we investigated the role of bulk porosity in controlling interfacial adhesion in structural systems inspired by the mussel plaque. Our main conclusions are summarized as follows:

(1) The heterogeneity of stresses on the adhesive interface plays a critical role in controlling the overall strength and ductility of the bonded porous plate. As the stress heterogeneity increases, the crack may get trapped more frequently in areas of low stress, leading to slower crack propagation, higher peak forces, larger ductility, and increased energy dissipation.

(2) The overall adhesion response depends on the details of the void distribution in the bulk even if the plate has the same void volume fraction and nearly the same elastic initial stiffness. Larger voids near the interface lead to higher stress heterogeneities and better overall response, in terms of peak force and ductility.

(3) The thickness of the horizontal strip adjacent to the interface plays a critical role in controlling the interfacial strength and failure mode. In particular, for a given void size, there is an optimum thickness for the horizontal strip that balances the edge crack and local failure modes leading to greatest overall peak force. This also suggests that having a horizontal strip may outperform the gecko-like pillar model that has been widely investigated in the literature.

Appendix: Semi-analytical model

We investigate two scenarios for interfacial separation (Fig. 3):

Propagation of An Edge Crack

The resulting differential equations for different cases will be one of the following forms:

(1) For debonded regions under the vertical webs

$$\frac{d^4v}{dx^4} = \frac{bK_v}{EI}(u_{cr} - v) \tag{A1}$$

which has a solution of the form

$$v = \frac{bK_v u_{cr}}{4\lambda^4 EI} + e^{\lambda x}\left(C_1\cos(\lambda x) + C_2\sin(\lambda x)\right)$$
$$+ e^{-\lambda x}\left(C_3\cos(\lambda x) + C_4\sin(\lambda x)\right) \tag{A2}$$

where

$$\lambda^4 = bK_v/4EI \qquad \text{(A3)}$$

(2) For damage process regions under the vertical webs

$$\frac{d^4v}{dx^4} = \frac{bK_v}{EI}(u_{cr} - v) - \frac{b\bar{\sigma}}{EI} \qquad \text{(A4)}$$

which has a solution of the form

$$v = \frac{bK_v u_{cr} - b\bar{\sigma}}{4\lambda^4 EI} + e^{\lambda x}\left(C_5\cos(\lambda x) + C_6\sin(\lambda x)\right) + e^{-\lambda x}\left(C_7\cos(\lambda x) + C_8\sin(\lambda x)\right) \qquad \text{(A5)}$$

where λ is the same as Eq. (5).

(3) For damage process regions under the void

$$\frac{d^4v}{dx^4} = \frac{-b\bar{\sigma}}{EI} \qquad \text{(A6)}$$

which has a solution of the form

$$v = \frac{-b\bar{\sigma}}{24EI}x^4 + C_9 x^3 + C_{10}x^2 + C_{11}x + C_{12} \qquad \text{(A7)}$$

(4) For debonded regions under the voids

$$\frac{d^4v}{dx^4} = 0 \qquad \text{(A8)}$$

which has a solution of the form

$$v = C_{13}x^3 + C_{14}x^2 + C_{15}x + C_{16} \qquad \text{(A9)}$$

The mathematical framework governing the beam deflection at any value of a is a combination of some or all of these equations depending on the location of the crack tip. Since each equation has four unknown constants, the total number of unknowns for any case is $4n$, where n is the number of equations in this specific case, in addition to the damage zone length l and the critical displacement u_{cr}.

The boundary conditions required to solve the equations are

$$\text{At} \quad x = 0, \ v' = 0, \ \text{and} \ v''' = 0 \qquad \text{(A10)}$$

$$\text{At} \quad x = a, \ v = v_o \qquad \text{(A11)}$$

$$\text{At} \quad x = a + l, \ v = v' = v'' = 0 \qquad \text{(A12)}$$

In addition, at the boundary between any two zones, the continuity of deformation, slope, bending moment, and shear force give 4 boundary conditions at $(n-1)$ boundaries. The total number of boundary conditions is $4n+2$ and the total number of equations is $4n+2$; hence, the system is solvable.

All the equations are nonlinear only in l. The equations are solved iteratively by (i) looping over a suitable range of l based on the analytical estimates of the process zone length [35], (ii) solving the resulting linear system, and then (iii) choosing the solution that minimizes the error.

Initiation of Local Cracks Under the Vertical Webs

While the edge crack propagates, the required top displacement u_{cr} increases, and hence the force in the inner leg increases. Cracks may initiate under the inner leg if the stresses exceed the cohesive strength. The onset of crack initiation in this case is shown in Fig. 3(b).

At the onset of failure under an inner leg, the governing equations are

$$\frac{d^4v}{dx^4} = \frac{bK_v}{EI}(u_{cr} - v) - \frac{b\bar{\sigma}}{EI}, \quad 0 \le x \le t_v/2 \qquad \text{(A13)}$$

$$\frac{d^4v}{dx^4} = -\frac{b\bar{\sigma}}{EI}, \quad t_v/2 \le x \le l \qquad \text{(A14)}$$

The solutions for these equations are the same as Eqs. (A8) and (A10). The total number of unknowns is 10. The boundary conditions are

$$\text{At} \quad x = 0, \ v = v_o, \ v' = v'' = 0 \qquad \text{(A15)}$$

$$\text{At} \quad x = l, \ v = v' = v'' = 0 \qquad \text{(A16)}$$

in addition to 4 continuity conditions at $x = t_v/2$ for a total of 10 conditions. The same solution technique is used to determine the critical displacement.

References

[1] Filippidi, E., DeMartini, D. G., De Molina, P. M., Danner, E. W., Kim, J., Helgeson, M. E., Waite, J. H., and Valentine, M. T., 2015, "The Microscopic Network Structure of Mussel (Mytilus) Adhesive Plaques," J. R. Soc. Interface, **12**(113), p. 20150827.

[2] Lee, B. P., Messersmith, P. B., Israelachvili, J. N., and Waite, J. H., 2011, "Mussel-Inspired Adhesives and Coatings," Annu. Rev. Mater. Res., **41**(1), pp. 99–132.

[3] Waite, J. H., 1987, "Nature's Underwater Adhesive Specialist," Int. J. Adhes. Adhes., **7**(1), pp. 9–14.

[4] Lee, H., Scherer, N. F., and Messersmith, P. B., 2006, "Single-Molecule Mechanics of Mussel Adhesion," Proc. Natl. Acad. Sci. U. S. A., **103**(35), pp. 12999–13003.

[5] Petrone, L., Kumar, A., Sutanto, C. N., Patil, N. J., Kannan, S., Palaniappan, A., Amini, S., Zappone, B., Verma, C., and Miserez, A., 2015, "Mussel Adhesion is Dictated by Time-Regulated Secretion and Molecular Conformation of Mussel Adhesive Proteins," Nat. Commun., **6**(1), pp. 1–12.

[6] Waite, J. H., 2017, "Mussel Adhesion—Essential Footwork," J. Exp. Biol., **220**(Pt. 4), pp. 517–530.

[7] Silverman, H. G., and Roberto, F. F., 2007, "Understanding Marine Mussel Adhesion," Mar. Biotechnol., **9**(6), pp. 661–681.

[8] Bell, E. C., and Gosline, J. M., 1996, "Mechanical Design of Mussel Byssus: Material Yield Enhances Attachment Strength," J. Exp. Biol., **199**, pp. 1005–1017.

[9] Desmond, K. W., Zacchia, N. A., Waite, J. H., and Valentine, M. T., 2015, "Dynamics of Mussel Plaque Detachment," Soft Matter, **11**(34), pp. 6832–6839.

[10] Ahn, B. K., 2017, "Perspectives on Mussel-Inspired Wet Adhesion," J. Am. Chem. Soc., **139**(30), pp. 10166–10171.

[11] Högberg, J. L., Sørensen, B. F., and Stigh, U., 2007, "Constitutive Behaviour of Mixed Mode Loaded Adhesive Layer," Int. J. Solids Struct., **44**(25–26), pp. 8335–8354.

[12] Furgiuele, F., Leonardi, A., Maletta, C., and Paulino, G. H., 2007, "Fracture Analysis of Adhesive Joints Using Intrinsic Cohesive Zone Models," Congress IGF19, Milan, Italy, July 2–4, pp. 77–84.

[13] Ha, K., Baek, H., and Park, K., 2015, "Convergence of Fracture Process Zone Size in Cohesive Zone Modeling," Appl. Math. Model., **39**(19), pp. 5828–5836.

[14] Dassault Systèmes Simulia, 2013, Abaqus Analysis User's Manual, 6.13th ed., Dassault Systèmes Simulia, Providence, RI.

[15] Turon, A., Dávila, C. G., Camanho, P. P., and Costa, J., 2007, "An Engineering Solution for Mesh Size Effects in the Simulation of Delamination Using Cohesive Zone Models," Eng. Fract. Mech., **74**(10), pp. 1665–1682.

[16] Yao, H., and Gao, H., 2010, "Gibson-Soil-Like Materials Achieve Flaw-Tolerant Adhesion," J. Comput. Theor. Nanosci., **7**(7), pp. 1299–1305.

[17] Daniel, R., Meindlhumer, M., Zalesak, J., Sartory, B., Zeilinger, A., Mitterer, C., and Keckes, J., 2016, "Fracture Toughness Enhancement of Brittle Nano-structured Materials by Spatial Heterogeneity: A Micromechanical Proof for CrN/Cr and TiN/SiOx multilayers," Mater. Des., **104**, pp. 227–234.

[18] Srivastava, A., Ponson, L., Osovski, S., Bouchaud, E., Tvergaard, V., and Needleman, A., 2014, "Effect of Inclusion Density on Ductile Fracture Toughness and Roughness," J. Mech. Phys. Solids, **63**(1), pp. 62–79.

[19] Hossain, M. Z., Hsueh, C. J., Bourdin, B., and Bhattacharya, K., 2014, "Effective Toughness of Heterogeneous Media," J. Mech. Phys. Solids, **71**(1), pp. 15–32.

[20] Lee, H., Lee, B. P., and Messersmith, P. B., 2007, "A Reversible Wet/Dry Adhesive Inspired by Mussels and Geckos," Nature, **448**(7151), pp. 338–341.

[21] Suzuki, T., Matsuzaki, R., Todoroki, A., and Mizutani, Y., 2015, "Prediction of the Macroscopic Fracture Toughness of a Composite/Adhesive Interface With Periodic Surface Microstructures," Int. J. Adhes. Adhes., **60**, pp. 16–22.

[22] Kim, W. S., Yun, I. H., Lee, J. J., and Jung, H. T., 2010, "Evaluation of Mechanical Interlock Effect on Adhesion Strength of Polymer metal Interfaces Using Micro-Patterned Surface Topography," Int. J. Adhes. Adhes., **30**(6), pp. 408–417.

[23] Glassmaker, N. J., Jagota, A., Hui, C.-Y., Noderer, W. L., and Chaudhury, M. K., 2007, "Biologically Inspired Crack Trapping for Enhanced Adhesion," Proc. Natl. Acad. Sci. U. S. A., **104**(26), pp. 10786–10791.

[24] Gorumlu, S., and Aksak, B., 2017, "Sticking to Rough Surfaces Using Functionally Graded Bio-Inspired Microfibres," R. Soc. Open Sci., **4**(6), p. 161105.

[25] Childers, A. S., Brodnik, N. R., and Faber, K. T., 2016, "Interfacial Frictional Stresses and Fracture Toughness of Biomorphic Graphite/Copper Interfaces," Mater. Lett., **174**, pp. 106–109.

[26] Del Campo, A., Greiner, C., and Arzt, E., 2007, "Contact Shape Controls Adhesion of Bioinspired Fibrillar Surfaces," Langmuir, **23**(20), pp. 10235–10243.

[27] Greiner, C., Del Campo, A., and Arzt, E., 2007, "Adhesion of Bioinspired Micropatterned Surfaces: Effects of Pillar Radius, Aspect Ratio, and Preload," Langmuir, **23**(7), pp. 3495–3502.

[28] Khaderi, S. N., Fleck, N. A., Arzt, E., and McMeeking, R. M., 2015, "Detachment of an Adhered Micropillar From a Dissimilar Substrate," J. Mech. Phys. Solids, **75**, pp. 159–183.

[29] Fleck, N. A., Khaderi, S. N., McMeeking, R. M., and Arzt, E., 2017, "Cohesive Detachment of an Elastic Pillar From a Dissimilar Substrate," J. Mech. Phys. Solids, **101**, pp. 30–43.

[30] Balijepalli, R. G., Fischer, S. C. L., Hensel, R., McMeeking, R. M., and Arzt, E., 2017, "Numerical Study of Adhesion Enhancement by Composite Fibrils With Soft Tip Layers," J. Mech. Phys. Solids, **99**, pp. 357–378.

[31] Launey, M. E., and Ritchie, R. O., 2009, "On the Fracture Toughness of Advanced Materials," Adv. Mater., **21**(20), pp. 2103–2110.

[32] Steenbrink, A. C., Van Der Giessen, E., and Wu, P. D., 1997, "Void Growth in Glassy Polymers," J. Mech. Phys. Solids, **45**(3), pp. 405–437.

[33] Crosby, A. J., Shull, K. R., Lakrout, H., and Creton, C., 2000, "Deformation and Failure Modes of Adhesively Bonded Elastic Layers," J. Appl. Phys., **88**(5), pp. 2956–2966.

[34] Creton, C., and Lakrout, H., 2000, "Micromechanics of Flat-Probe Adhesion Tests of Soft Viscoelastic Polymer Films," J. Polym. Sci. Part B Polym. Phys., **38**(7), pp. 965–979.

[35] Williams, J. G., and Hadavinia, H., 2002, "Analytical Solutions for Cohesive Zone Models," J. Mech. Phys. Solids, **50**(4), pp. 809–825.